Comparative Evaluation of Model-Free and Model-Based Predictive Control for a Wind-Battery DC Microgrid Supplying a Surface Water Heat Pump

Joyce Assaf, Mamadou-Baïlo Camara, Damien Guilbert, and Brayima Dakyo
Groupe de Recherche en Electrotechnique et Automatique du Havre (GREAH)
Université Le Havre Normandie
Le Havre, Normandie, France
joyce.assaf@univ-lehavre.fr, camaram@univ-lehavre.fr, damien.guilbert@univ-lehavre.fr, brayima.dakyo@univ-lehavre.fr

***Abstract*—This study evaluates model-free predictive control (MFPC) and feedforward (FF) model predictive control (MPC) applied to a nonlinear DC microgrid consisting of a wind energy conversion system (WECS) and a battery energy storage system (BESS) supplying two surface water heat pumps (SWHPs) operating in parallel. FF-MPC relies on explicit converter models and a PI outer loop, whereas MFPC employs an ultra-local model with online disturbance estimation, eliminating the need for precise system identification. Both strategies are implemented on boost and bidirectional buck-boost converters and evaluated under variable wind speed and dynamic thermal load profiles. Simulation results show that MFPC substantially outperforms FF-MPC in terms of DC bus voltage regulation and wind turbine (WT) inductor current tracking accuracy, at the cost of a moderate increase in battery current deviation and power imbalance.**

***Index Terms*—Model-Free Predictive Control, Model Predictive Control, DC Microgrid, Wind Turbine, Battery Energy Storage System.**

I. Introduction

The decarbonization of the heating sector represents one of the most pressing challenges in the energy transition, as thermal applications account for a significant share of global final energy consumption [1]. Surface water heat pumps (SWHPs) have emerged as a highly efficient solution for low-carbon heating, leveraging the thermal inertia of water bodies to achieve coefficients of performance (COP) well above conventional systems [2]. When coupled with renewable energy sources (RESs) through a DC microgrid architecture, SWHPs offer a pathway toward fully decarbonized, self-sufficient thermal systems [3].

In this context, DC microgrids integrating a wind energy conversion system (WECS) and a battery energy storage system (BESS) to supply SWHPs represent a particularly promising configuration, combining wind energy intermittency management with efficient thermal load supply [4]. This configuration is also aligned with the recent shift toward integrated wind–storage and flexible-load systems, where battery storage and coordinated control are increasingly required to smooth wind power variability, enhance flexibility, and support reliable renewable energy integration [5].

However, such systems impose stringent control requirements at the power converter level [6], [7]. Wind speed variability induces rapid fluctuations in the WECS output power, while load switching events from the SWHP compressor generate transient disturbances on the DC bus. Maintaining DC bus voltage regulation and accurate inductor current tracking in both the boost converter interfacing the WECS and the bidirectional DC-DC converter (BDC) managing the BESS under these dynamic conditions requires advanced control strategies capable of fast response and robustness to operating point variations [8].

Finite control set model predictive control (FCS-MPC) has established itself as a leading approach for converter-level control in DC microgrids, offering fast dynamic response, intuitive multi-objective cost function formulation, and natural compatibility with the discrete switching nature of power converters [9]. Conventional MPC relies on an explicit discrete-time model of the converter to predict future states and select the optimal switching action [10]. In renewable microgrids, uncertainties in RESs generation, thermal load demand, and converter parameters can degrade prediction accuracy and lead to suboptimal control actions. This limitation becomes more critical in islanded systems, where fast power mismatches must be compensated locally by the BESS to preserve DC bus stability [11].

To overcome this limitation, model-free predictive control (MFPC) has been proposed as an alternative framework based on the ultra-local model concept [12]. Rather than relying on a physical model of the converter, MFPC estimates a lumped disturbance term online using only input-output measurements, which absorbs parametric uncertainty, nonlinearities, and unmodeled dynamics. This approach removes the need for system identification or parameter tuning, making it inherently robust to model mismatch.

While MFPC has been studied for motor drives [13] and DC–DC converters [14], this paper compares MFPC to feed-

forward (FF)-MPC in a WECS–BESS DC microgrid supplying two parallel SWHPs, under a realistic variable wind profile and a high-resolution dynamic thermal load profile with power measurements sampled every 5 seconds. The main contributions of this work are as follows:

- A converter-level comparative study of FF-MPC and MFPC applied simultaneously to both the WECS boost converter and the BESS bidirectional DC-DC converter in a wind–battery DC microgrid, evaluating DC bus voltage regulation, inductor current tracking, and power management under dynamic operating conditions.
- A contribution to the growing body of research on surface water heat pumps as DC microgrid loads, demonstrating their integration with wind-based generation and battery storage in a fully converter-controlled architecture.
- The use of a high-resolution thermal load profile derived from real SWHP operating data, with thermal power measurements recorded every 5 seconds, producing a highly dynamic electrical demand profile that constitutes a realistic and challenging benchmark for converter-level control evaluation.

The remainder of this paper is organized as follows. Section II presents the DC microgrid configuration and the implemented converter control strategies. Section III discusses the MATLAB/Simulink results using wind data from the Grieneko pilot site and real thermal load data from an aquathermal site in Belgium, both within the 'WaterWarmth project'. Section IV concludes the paper and outlines future work.

II. DC MICROGRID CONFIGURATION AND CONTROL

The studied system, displayed in Fig. 1, is an islanded DC microgrid comprising a 35 kW WECS, a 35 kWh BESS, and two 30 kW SWHPs connected to a common DC bus. The WECS includes a permanent magnet synchronous generator (PMSG), a diode rectifier, and a boost converter, while the BESS is interfaced through a buck-boost DC-DC BDC. The DC bus voltage reference $V_{\text{bus}}^{\text{ref}}$ is 1000 V.

Two predictive control strategies, FF-MPC and MFPC, are evaluated under identical operating conditions using the same wind and thermal load profiles. FF-MPC relies on a physics-based model with a cascaded PI structure, making it sensitive to parameter uncertainties. In contrast, MFPC integrates disturbance estimation directly into the control law, enabling improved response under fast-changing conditions.

A. Wind Turbine Boost Control

The wind turbine (WT) is interfaced with the DC bus through the boost converter, as shown in Fig. 2. The power reference is converted into an inductor current reference as in (1):

$$i_{L,\text{WT}}^{\text{ref}} = \frac{P_{\text{WT}}^{\text{ref}}}{V_{\text{WT,in}}} \tag{1}$$

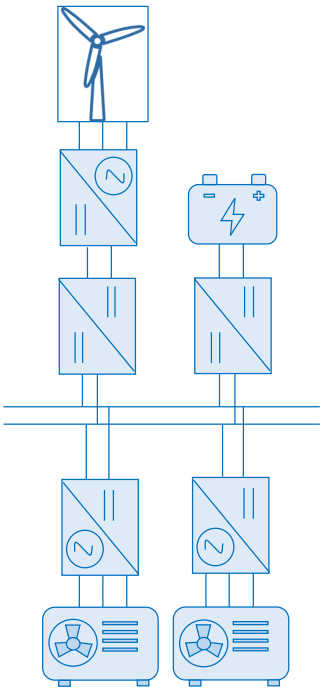

Fig. 1. DC microgrid configuration.

where $V_{\text{WT,in}}$ is the rectified voltage at the output of the diode bridge and the reference power is found according to (2):

$$P_{\text{WT}}^{\text{ref}} = \begin{cases} 0, & v_{\text{w}} \le v_{\text{cut-in}} \text{ or } v_{\text{w}} \ge v_{\text{cut-out}}, \\ K_{\text{opt}} \cdot \omega_{\text{m}}^3, & v_{\text{cut-in}} < v_{\text{w}} < v_{\text{cut-out}} \text{ and } \omega_{\text{m}} \le \omega_{\text{r}}, \\ P_{\text{WT,rated}}, & v_{\text{cut-in}} < v_{\text{w}} < v_{\text{cut-out}} \text{ and } \omega_{\text{m}} > \omega_{\text{r}}. \end{cases} \tag{2}$$

where K_{opt} is the optimal power coefficient derived from the WT aerodynamic characteristics as reported in [15], and ω_{m} is the rotor mechanical speed.

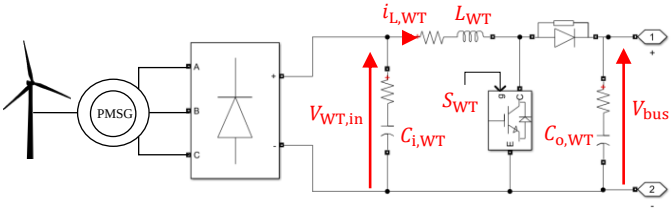

Fig. 2. Wind energy conversion chain.

1) Feedforward Model Predictive Control: The FF-MPC relies on an explicit discrete-time model of the converter to predict the inductor current. The inductor current is regulated using an FCS-MPC approach. At each sampling instant, the controller evaluates the two possible switching states of the boost converter and predicts the corresponding inductor current as in (3):

$$i_{L,\mathrm{WT}}[k+1] = i_{L,\mathrm{WT}}[k] + \frac{T_\mathrm{s}}{L_\mathrm{WT}} \cdot \Big(V_{\mathrm{WT,in}}[k] - R_{L,\mathrm{WT}} \cdot i_{L,\mathrm{WT}}[k] - V_\mathrm{bus}[k] \cdot \big(1 - S_\mathrm{WT}[k]\big) \Big) \tag{3}$$

where $S_\mathrm{WT} \in \{0,1\}$ represents the switching state, T_s the sampling time, R_L the inductor's resistance, and V_bus the DC bus voltage.

A cost function is defined to minimize the current tracking error while reducing switching frequency as in (4):

$$g_\mathrm{WT} = \big(i^\mathrm{ref}_{L,\mathrm{WT}}[k] - i_{L,\mathrm{WT}}[k+1]\big)^2 + w_f^\mathrm{WT} \cdot \big(S_\mathrm{WT}[k] - S_\mathrm{WT}[k-1]\big)^2 \tag{4}$$

where w_f^WT is a weighting factor and $S_\mathrm{WT}[k-1]$ is the switching state applied at the previous sampling instant.

2) Model Free Predictive Control: In contrast, MFPC does not rely on an explicit model of the converter. Instead, it uses an ultra-local model to represent the system dynamics as expressed in (5):

$$i_{L,\mathrm{WT}}[k+1] = i_{L,\mathrm{WT}}[k] + T_\mathrm{s} \cdot \Big(\hat{F}_\mathrm{WT}[k] + G_\mathrm{WT} \cdot S_\mathrm{WT}[k] \Big) \tag{5}$$

where $\hat{F}$ represents the aggregated effect of unknown dynamics and disturbances, estimated at each sampling instant, and G_WT is the control gain. G_WT is selected empirically to match the sensitivity of the inductor current to the switching action.

The optimal switching state is selected by minimizing the cost, computed in (4), which is the same function used for both MFPC and FF-MPC.

B. Battery Buck-boost Control

The battery pack (350 V, 100 Ah) is interfaced with the DC bus through a buck–boost BDC, as shown in Fig. 3. The BDC operates in boost mode during battery discharge and in buck mode during battery charging.

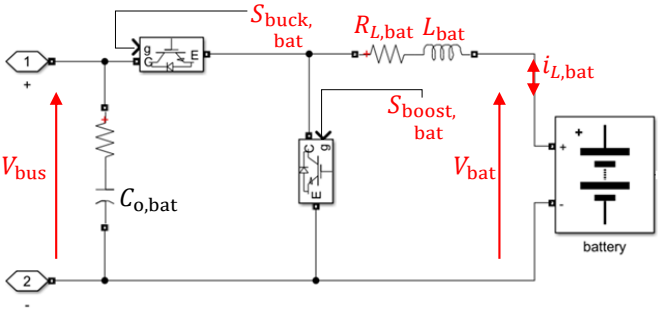

Fig. 3. Battery energy storage system with its bidirectional buck-boost converter.

1) Feedforward Model Predictive Control: For FF-MPC, the BESS uses an outer DC bus voltage loop where a PI controller with anti-windup generates $i^\mathrm{PI}_\mathrm{bat}$. An FF term $i^\mathrm{FF}_\mathrm{bat}$, based on instantaneous power imbalance, is added to improve disturbance rejection. The battery current reference is thus given by (6):

$$i^\mathrm{ref}_{L,\mathrm{bat}}[k] = i^\mathrm{PI}_\mathrm{bat}[k] + i^\mathrm{FF}_\mathrm{bat}[k] \tag{6}$$

The one-step-ahead inductor current prediction is then computed using a forward Euler discretization of the inductor dynamics as in (7):

$$i_{L,\mathrm{bat}}[k+1] = i_{L,\mathrm{bat}}[k] + \frac{T_\mathrm{s}}{L_\mathrm{bat}} \cdot \Big(V_\mathrm{mode}[k] - R_{L,\mathrm{bat}} \cdot i_{L,\mathrm{bat}}[k] - \big(1 - S_\mathrm{bat}[k]\big) \cdot V_\mathrm{bus}[k] \Big) \tag{7}$$

where V_mode is equal to V_bat in boost mode and to $V_\mathrm{bus} - V_\mathrm{bat}$ in buck mode.

A cost function is defined as in (8), where the first term penalizes the current tracking error and the second term penalizes switching transitions to reduce the average switching frequency.

$$g_\mathrm{bat} = \big(i^\mathrm{ref}_{L,\mathrm{bat}}[k] - i_{L,\mathrm{bat}}[k+1]\big)^2 + w_\mathrm{f}^\mathrm{bat} \cdot \big(S_\mathrm{bat}[k] - S_\mathrm{bat}[k-1]\big)^2 \tag{8}$$

where $w_\mathrm{f}^\mathrm{bat}$ is a weighting factor and $S_\mathrm{bat}[k-1]$ is the switching state applied at the previous sampling instant.

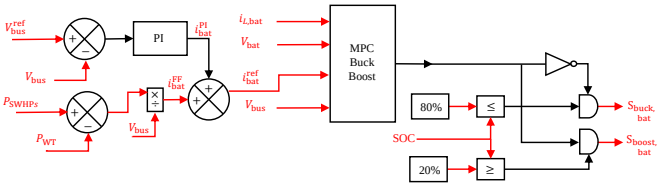

Fig. 4. BDC control scheme with FF–MPC and SOC-based mode selection.

2) Model Free Predictive Control: For the battery reference current, the inductor reference current is directly computed from the DC bus voltage using (9):

$$i^\mathrm{ref}_{L,\mathrm{bat}}[k] = \frac{-\hat{F}_{V,\mathrm{bat}}[k] + K_\mathrm{pV} \cdot \big(V^\mathrm{ref}_\mathrm{bus} - V_\mathrm{bus}[k]\big)}{G_{V,\mathrm{bat}}} \tag{9}$$

where $G_{\mathrm{V,bat}}$ is the input gain associated with the ultra-local voltage model, K_pV is the voltage error gain, and $\hat{F}_{\mathrm{V,bat}}[k]$ is the lumped voltage-increment term estimated online at each sampling instant.

The optimal switching state is selected by minimizing the cost function computed in (8), which is the same function used for both MFPC and FF-MPC. The main parameters used in the simulations are summarized in Table I.

TABLE I
PARAMETERS USED IN THE SIMULATIONS.

Parameter	Symbol	Value
WT boost inductor	L_{WT}	1 mH
BESS BDC inductor	L_{bat}	1 mH
WT output capacitance	$C_{\mathrm{o,WT}}$	3300 μF
BESS output capacitance	$C_{\mathrm{o,bat}}$	3300 μF
WT input capacitance	$C_{\mathrm{in,WT}}$	180 μF
Switching frequency	f_{s}	10 kHz

III. RESULTS AND DISCUSSION

The DC bus voltage behavior under both control strategies is illustrated in Fig. 5. The FF-MPC exhibits oscillations ranging from 985 V to 1015 V around the nominal 1000 V (peak-to-peak ripple of approximately 3%). Although within the acceptable 5% range, they persist under all wind conditions, indicating limited disturbance rejection capability. In contrast, the MFPC achieves significantly improved voltage regulation, maintaining the DC bus voltage between 999 V and 1002 V (peak-to-peak ripple of approximately 0.3%). This improvement stems from the ultra-local formulation, where the disturbance term $\hat{F}$ is estimated and compensated at each sampling instant, enabling fast and inherent disturbance rejection. As a result, the DC bus voltage root mean square error (RMSE) is reduced from 3.1 V to 0.39 V, demonstrating the superior robustness of the MFPC approach.

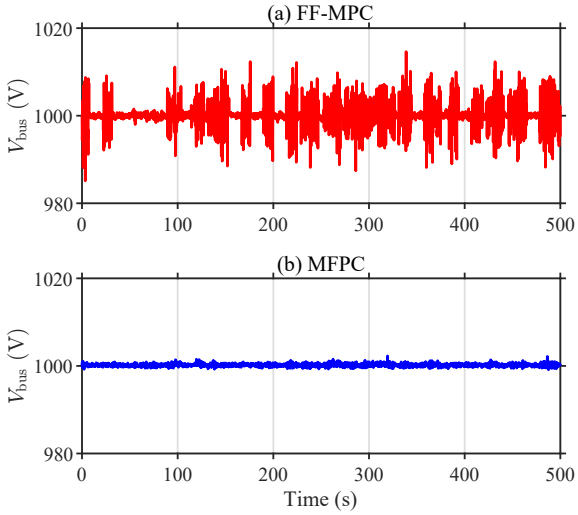

Fig. 5. DC bus voltage regulation performance under (a) FF-MPC and (b) MFPC over the complete simulation period.

The battery inductor current tracking performance is illustrated in Fig. 6. Under FF-MPC (Fig. 6(a)), the inductor current $i_{L,\mathrm{bat}}$ closely follows its reference $i_{L,\mathrm{bat}}^{\mathrm{ref}}$ with relatively low tracking error and smooth dynamic response. In comparison, the MFPC (Fig. 6(b)) maintains acceptable tracking performance but exhibits slightly larger deviations and increased oscillations, particularly during fast operating transitions. Quantitatively, the battery current RMSE increases from 26.8 A under FF-MPC to 27.4 A under MFPC (+2%), while the maximum tracking error rises from 55.7 A to

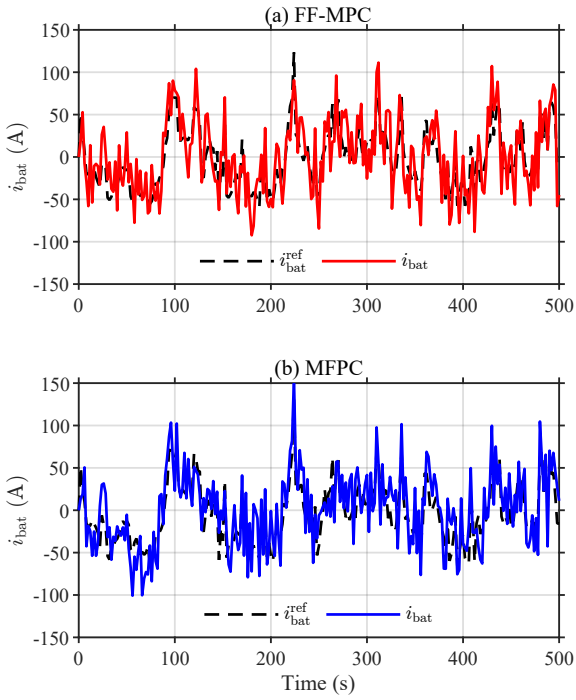

Fig. 6. Battery current tracking performance under (a) FF-MPC and (b) MFPC over the complete simulation period.

64.3 A (+15%). Despite this moderate degradation, the overall behavior remains well controlled, and the current follows its reference without drift. Despite the absence of an explicit converter model, MFPC maintains effective battery current regulation with bounded tracking error throughout all operating conditions.

The WT inductor current tracking performance for both control strategies is presented in Fig. 7. Under FF-MPC (Fig. 7(a)), $i_{L,\mathrm{WT}}$ exhibits significant deviations from its reference $i_{L,\mathrm{WT}}^{\mathrm{ref}}$, characterized by high-frequency oscillations and large tracking errors across the entire operating range. This is because the model is sensitive to parameter mismatch and fast operating variations, limiting its tracking accuracy under dynamic conditions. In contrast, the MFPC (Fig. 7(b)) achieves substantially improved tracking performance, with $i_{L,\mathrm{WT}}$ closely following $i_{L,\mathrm{WT}}^{\mathrm{ref}}$ and exhibiting reduced oscillations. This improvement is enabled by the ultra-local model formulation, which continuously estimates and compensates unknown dynamics through the disturbance term. Quantitatively, the WT current RMSE is reduced from 23.1 A to 7.4 A (−68%), while the maximum tracking error decreases from 50.1 A to 15.1 A (−70%). These results confirm the superior robustness and tracking capability of the MFPC under identical operating conditions.

Fig. 8 illustrates the DC microgrid response under a severe wind speed disturbance occurring between 395 s and 425 s. As shown in Fig. 8(a), the wind speed rapidly increases from approximately 10 m/s to nearly 17.8 m/s before progressively decreasing again, producing significant variations in the WECS output power and therefore a highly challenging operating

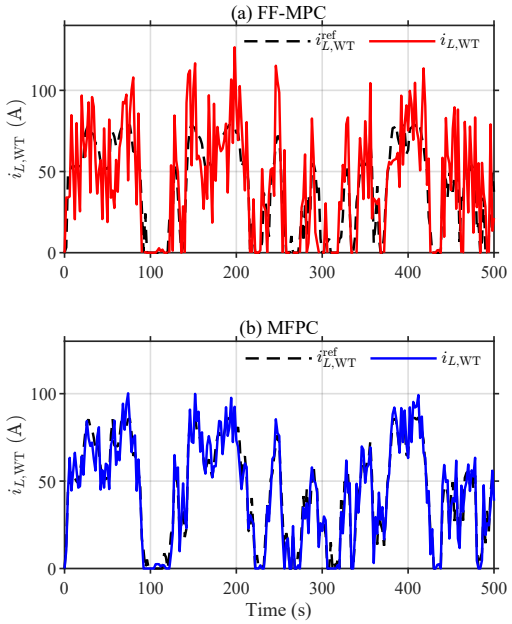

Fig. 7. WT inductor current tracking performance under (a) FF-MPC and (b) MFPC over the complete simulation period.

condition for DC bus voltage regulation. The corresponding DC bus voltage responses are presented in Fig. 8(b). Under FF-MPC, the DC bus voltage exhibits pronounced oscillations and repeated voltage excursions around the 1000 V reference, with fluctuations ranging approximately from 994 V to 1007 V during the disturbance interval. In contrast, the MFPC maintains the DC bus voltage tightly regulated around the reference value with significantly reduced oscillations throughout the entire transient event. The associated WT inductor current tracking performances are shown in Fig. 8(c) and Fig. 8(d). Under FF-MPC, $i_{L,\mathrm{WT}}$ exhibits strong oscillatory behavior and large deviations from $i^{\mathrm{ref}}_{L,\mathrm{WT}}$, particularly during the rapid wind speed increase between 405 s and 415 s. These tracking errors result from the sensitivity of the MPC to fast operating point variations and converter parameter mismatch under highly dynamic wind conditions. In contrast, the MFPC achieves substantially improved WT current tracking, with $i_{L,\mathrm{WT}}$ closely following $i^{\mathrm{ref}}_{L,\mathrm{WT}}$ while exhibiting significantly reduced oscillations.

Fig. 9 illustrates the dynamic response of the DC microgrid under rapid SWHP load variations occurring between 180 s and 210 s. As shown in Fig. 9(a), the thermal demand of the parallel SWHPs exhibits multiple abrupt transitions, including several high-power pulses reaching approximately 200 kW. These thermal fluctuations generate the corresponding electrical power demand shown in Fig. 9(b), where the electrical consumption of the SWHPs rapidly varies between approximately 10 kW and 53 kW. The resulting DC bus voltage responses under both control strategies are presented in Fig. 9(c). During the disturbance interval, the FF-MPC exhibits pronounced voltage oscillations around the 1000 V reference, with repeated overshoots and undershoots caused by the rapid

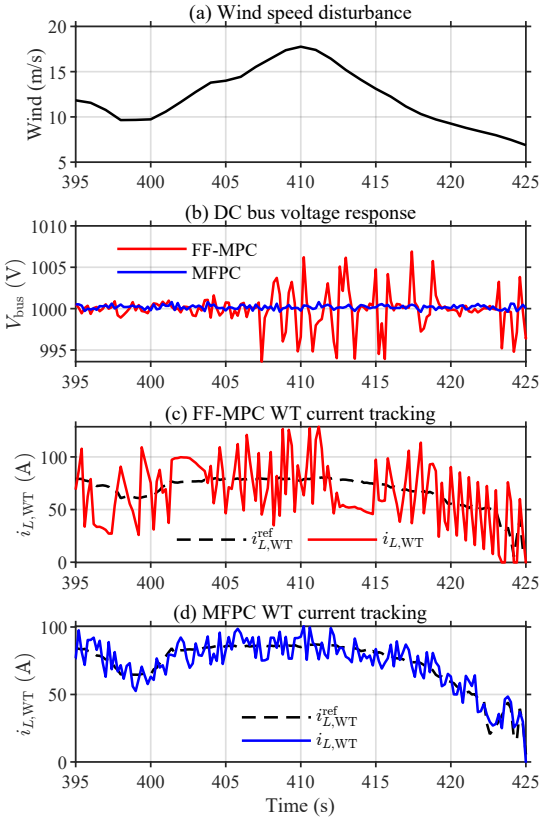

Fig. 8. (a) Wind speed disturbance and corresponding (b) DC bus voltage response, (c) WT current tracking under FF-MPC, and (d) WT current tracking under MFPC between 395 s and 425 s.

load switching events. In contrast, the MFPC maintains the DC bus voltage tightly regulated with substantially reduced fluctuations throughout the transient period.

The corresponding battery current tracking performances are presented in Fig. 9(d) and Fig. 9(e). Under FF-MPC, i_{bat} exhibits significant oscillations and large tracking deviations from $i^{\mathrm{ref}}_{\mathrm{bat}}$, particularly during the high-power load transitions between 190 s and 200 s. In comparison, the MFPC maintains effective battery current tracking with smoother behavior and reduced oscillatory excursions despite the absence of an explicit converter model or cascaded PI voltage loop. Although some tracking deviations remain under severe transient conditions, the MFPC preserves substantially tighter DC bus voltage regulation throughout the entire disturbance interval.

In addition to tracking-based metrics, an energy-based analysis was conducted using the power imbalance between generation, storage, and load. The results indicate that the MFPC exhibits a higher root mean square (RMS) power imbalance compared to the FF-MPC, increasing from 13.6 kW to 18.3 kW (+35%). This behavior is mainly due to the absence of explicit power smoothing in MFPC, which prioritizes instantaneous DC bus voltage compensation over coordinated power balancing, leading to faster regulation but larger battery current excursions. Table II summarizes the key performance metrics.

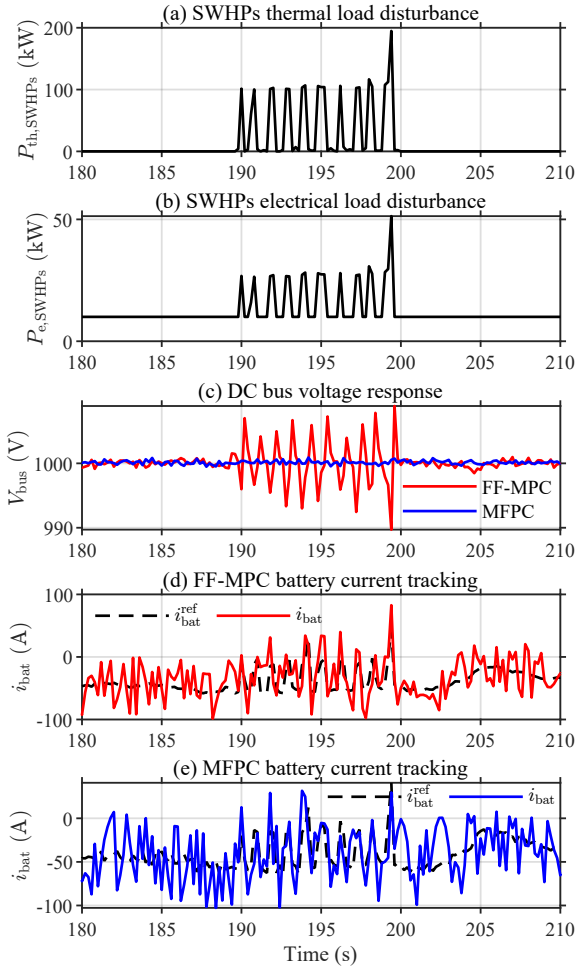

Fig. 9. (a) Thermal load disturbance, derived (b) electrical power demand of the SWHPs, corresponding (c) DC bus voltage response, battery current tracking under (d) FF-MPC and (e) MFPC between 180 s and 210 s.

TABLE II
PERFORMANCE COMPARISON BETWEEN FF-MPC AND MFPC.

Metric	FF-MPC	MFPC	Change
DC bus voltage RMSE (V)	3.1	0.39	−87%
BESS current RMSE (A)	26.8	27.4	+7%
WT current RMSE (A)	23.1	7.4	−68%
Power Imbalance RMS (kW)	13.6	18.3	+35%

IV. Conclusion and Future Work

This paper compared FF-MPC and MFPC for converter-level control in a DC microgrid integrating a WECS, a BESS, and two parallel SWHPs. MFPC demonstrated clear advantages in DC bus voltage regulation and WT current tracking, achieving an 87% reduction in voltage RMSE and a 68% reduction in WT current RMSE relative to FF-MPC. These gains stem from the inherent disturbance rejection of the ultra-local model formulation, which continuously estimates and compensates unknown dynamics without relying on converter parameters. The trade-offs are modest: battery current RMSE increases by 7% and power imbalance RMS by 35%, while maintaining satisfactory load supply and overall system operation. These results position MFPC as a particularly suitable strategy for DC microgrids subject to renewable variability and parameter uncertainty. Future work will explore advanced converter topologies to further enhance efficiency, scalability, and dynamic performance under extended operating scenarios.

Acknowledgment

This work was conducted at the GREAH laboratory, Université Le Havre Normandie, particularly by the research team on renewable energies and storage systems (MERS). This work was carried out within the framework of Interreg WaterWarmth project co-funded by the European Union. The authors would like to thank the European Union and Université Le Havre Normandie for their financial support.

References

[1] E. J. Sobczyk, W. Sobczyk, T. Olkuski, and M. Ciepiela, "Assessing the pace of decarbonization in EU countries using multi-criteria decision analysis," *Energies*, vol. 19, no. 1, p. 243, 2026.

[2] S. Bouma, A. Depoorter, J. Santier, and L. Fauvin, "How to decarbonize heating and cooling? The case of (marine) aquathermal energy as a solution for sustainable heating and cooling in the built environment," in *Rencontres de l'Ingénierie Maritime 2024*, 2024.

[3] J. Assaf, M.-B. Camara, D. Guilbert, and B. Dakyo, "PV-battery powered surface water heat pump system control and simulation," in *2025 14th International Conference on Renewable Energy Research and Applications (ICRERA)*, 2025, pp. 270–275, doi: 10.1109/ICRERA66237.2025.11283957.

[4] J. Assaf, M.-B. Camara, D. Guilbert, and B. Dakyo, "Energy management of a surface water heat pump powered by wind and a battery system," in *GREEN 2025, The Tenth International Conference on Green Communications, Computing and Technologies*, Barcelona, Spain, 2025, pp. 16–21.

[5] Global Wind Energy Council (GWEC), "Global Wind Report 2026," GWEC, Brussels, Belgium, 2026.

[6] S. D. Sandeep, S. Mohanty, S. B. Mohanty, and P. S. Puhan, "A comprehensive review on DC microgrid control and energy management strategies," Results in Engineering, vol. 26, p. 105479, 2025.

[7] M. Khalid, "Smart grids and renewable energy systems: Perspectives and grid integration challenges," Energy Strategy Reviews, vol. 51, p. 101299, 2024.

[8] M. Batool, W. Hassan, and D. D.-C. Lu, "Review of advanced control strategies for isolated DC-DC converters in DC microgrids," IEEE Access, 2025.

[9] O. Babayomi, R. Madonski, Z. Zhang, J. Rodriguez, I. Davidson, and D.-S. Kim, "Robust model predictive control of converter-based microgrids," IEEE Transactions on Power Electronics, 2025.

[10] C. B. Nzoundja Fapi, M. L. Touré, M.-B. Camara, and B. Dakyo, "Control strategy for DC micro-grids in heat pump applications with renewable integration," Electronics, vol. 14, no. 1, p. 150, 2025.

[11] E. Yaghoubi, E. Yaghoubi, M. R. Maghami, J. Rahebi, M. Z. Jahromi, R. Ghadami, and Z. Yusupov, "A systematic review and meta-analysis of model predictive control in microgrids: Moving beyond traditional methods," *Processes*, vol. 13, no. 7, p. 2197, 2025.

[12] M. Fliess and C. Join, "Model-free control," *International Journal of Control*, vol. 86, no. 12, pp. 2228–2252, 2013.

[13] C. Zhou, Y. Zhang, and H. Yang, "Model-free predictive control of motor drives: A review," CES Transactions on Electrical Machines and Systems, vol. 9, no. 1, pp. 76–90, 2025.

[14] A. Maureira, S. Riffo, E. Ibáñez, C. González-Castaño, M. Rivera, C. Guarnizo-Lemus, A. M. Alcaide, and C. Restrepo, "Kalman filter-based model-free predictive control of classical dc-dc power converters," *IEEE Open Journal of the Industrial Electronics Society*, 2025.

[15] D. Ikni, M. B. Camara, A. Payman, and B. Dakyo, "Dynamic control of wind energy conversion system," in *2013 Eighth International Conference and Exhibition on Ecological Vehicles and Renewable Energies (EVER)*, 2013, pp. 1–5.